An Emissivity Modulation Method for Spatial Enhancement of Ther mal Satellite Images in Urban Heat Island Analysis

Janet Nichol

Abstract

*This study examines and validates a technique for spatial enhancement of thermal satellite images for urban heat island analysis, using a nighttime ASTER satellite image. The technique, termed Emissivity Modulation, enhances the spatial resolution while simultaneously correcting the image derived temperatures for emissivity differences of earth surface materials. A classified image derived from a higher resolution visible wavelength sensor is combined with a lower resolution thermal image in the emissivity correction equation in a procedure derived from the Stephan Bolzmann law. This has the effect of simultaneously correcting the image-derived "Brightness Temperature" (**Tb**) to the true Kinetic Temperature (**Ts**), while enhancing the spatial resolution of the thermal data. Although the method has been used for studies of the urban heat island, it has not been validated by comparison with "in situ" derived surface or air temperatures, and researchers may be discouraged from its use due to the fact that it creates sharp boundaries in the image. The emissivity modulated image with 10 m pixel size was found to be highly correlated with 18 in situ surface and air temperature measurements and a low Mean Absolute Difference of 1 K was observed between image and in situ surface temperatures. Lower accuracies were obtained for the **Ts** and **Tb** images at 90 m resolution. The study demonstrates that the emissivity modulation method can increase accuracy in the computation of kinetic temperature, improve the relationship between image values and air temperature, and enable the observation of microscale temperature patterns.*

Introduction

Rising temperatures in tropical and sub-tropical cities mean that planners now need to consider adverse health effects such as respiratory problems due to increase in ground level ozone, and heat stress, and heat-induced mortality in their planning strategies. Measures include the influence of street layout, building geometry, and surface materials. Due to the low resolution of the current thermal satellite sensors, Landsat TM (120 m), Landsat ETM+ (60 m), and ASTER (90 m), there are no spatially detailed climatic data covering whole cities. Furthermore, the scan line corrector problem experienced by Landsat ETM+ since 2003, the lack of a thermal infrared band in the Landsat Data Continuity Mission and the potentially long development period for NASA's newly announced Hyperspectral Infrared Imager (Nichol *et al.*, 2007), means that the highest resolution obtainable available from thermal satellite sensors in the foreseeable future is 90 m from ASTER.

This study examines and validates a simple technique for enhancing the spatial resolution of ASTER thermal images, while simultaneously correcting the image derived temperatures for emissivity differences of surface materials. The method combines a classified image derived from a higher resolution visible wavelength sensor, and a set of externally derived emissivity values with a lower resolution thermal image. It effectively ratios the visible and thermal datasets in the emissivity correction equation in a procedure derived from the Stephan Bolzmann law. This has the effect of simultaneously correcting the image-derived "Brightness Temperature" (**Tb**) to the actual Kinetic Temperature of the surface (**Ts**), while enhancing the spatial resolution of the thermal data. Although the method has been used for studies of urban microclimate due to its apparent ability to depict detailed temperature patterns, it has not been validated by comparison with *in situ* derived surface or air temperatures. The present study uses a nighttime ASTER image covering both urban and rural areas of Hong Kong, and compares the emissivity modulated (EM) image to eighteen *in situ* surface temperatures collected at the image time to examine the extent of the accuracy improvement, if any, in the context of urban heat island analysis.

Due to the difficulty of synchronizing ground measurement with image acquisition, the few studies which have verified satellite-derived surface temperatures with substantial *in situ* contact surface temperatures have been for sensors with high temporal resolution, but incidentally, low spatial resolution (Ulivieri *et al.*, 1992; Prata, 1994). Those studies examining higher spatial resolution sensors have measured only near-surface radiance representing **Tb**, from towers and helicopters (Goetz *et al.*, 1997; Li *et al.*, 2004; Rigo *et al.*, 2006), which tends to be more variable than the actual surface temperature (Prata, 1994; Figure 1). The results of both types of studies suggest that the derived accuracies do not vary according to the spatial resolution if the field of view of the image data is comparable to the ground area being measured. For example, Prata (1994) obtained very high correlations between AVHRR-derived **Ts**

Department of Land Surveying and Geo-Informatics, The Hong Kong Polytechnic University, Kowloon, Hong Kong (lsjanet@polyu.edu.hk).

Photogrammetric Engineering & Remote Sensing
Vol. 75, No. 5, May 2009, pp. 547–556.

0099-1112/09/7505–0547/$3.00/0

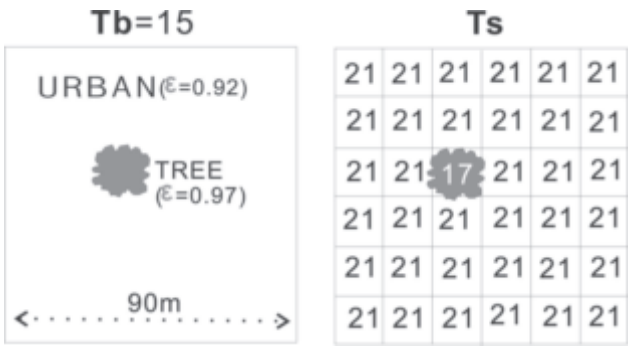

Figure 1. Effect of pixel block membership on fragmented land cover types in Emissivity Modulation. A tree canopy in a dominantly urban pixel block will have the same high **Tb** value as urban before emissivity modulation. This erroneously high apparent temperature will not be corrected by the EM process, and the temperature of the tree pixel will be further increased, though to a lesser extent than that of urban pixels.

and *in situ* measurements when contact thermistors were deployed over an area of approximately 1 km^2, corresponding to the size of an AVHRR pixel. Li *et al.* (2004) and Rigo *et al.* (2006) support this assertion, and Rigo *et al.* (2006) recommend higher spatial resolution sensors for urban climatology due to the greater size correspondence between image pixels and urban features.

Spatial Enhancement of Ther mal Images

Two groups of methods have been proposed to enhance the detail within thermal image pixels. These are (a) a spectral unmixing approach which uses several thermal bands to retrieve sub-pixel constituents (Dozier, 1981; Gillespie, 1992; Collins *et al.*, 2001), and (b) pixel block modulation (Guo and McMoore, 1998) which incorporates visible wavebands of the same sensor or ancillary information at a higher resolution, to enhance a single thermal band.

Spectral Unmixing

In spectral unmixing, the objective is to retrieve a set of component fractions and one or more temperatures for each thermal pixel, based on the thermal spectrum of the components and known emissivities from a spectral library (Gillespie, 1992; Collins, 2001). Temperatures are obtained by regression of endmember fractions against a virtual cold endmember derived from the image wavebands. However, the derivation of thermal endmembers suffers from temporal and spatial variability of components in relation to patterns of insolation and cooling, and the applicability of the model to real data is limited by non-linearity between temperatures and component fractions.

Another spectral unmixing approach "image sharpening" introduced by Gustavson *et al.* (2003) to retrieve stream water temperatures uses image-based data alone, without reference to thermal endmembers. In their study, four land-cover endmembers were derived from spectral unmixing of ASTER's 15 m VNIR pixels. The fractions of these endmembers within each larger (90 m thermal) pixel block were then summed, and regressed against each pixel's thermal radiance within a 5*5 − 90 m thermal image kernel. Thus, the thermal radiance of the 90 m fractions was obtained. This radiance was then multiplied by the corresponding 15 m fraction amounts and summed across the four endmember fraction images to give thermal radiance at 15 m. The temperatures so derived require further refinement using multiple thermal bands in a Temperature Emissivity Separation (TES) algorithm (Gillespie *et al.*, 1998), due to the non-linearity referred to above. In general, the outputs from spectral unmixing are computationally complex and have not been substantially verified. These constraints would be even greater for night scenes due to the lack of spectral contrast between bands, thus the difficulty of defining meaningful endmembers.

Pixel Block Modulation

The second group of methods incorporating ancillary data of higher resolution is computationally simpler, and applicable to a single thermal band. Guo and Moore (1998) proposed the Pixel Block Intensity Modulation method, which uses the higher resolution reflective bands of a sensor to identify topographic variations within a lower resolution thermal band pixel block. Using the observed illumination differences on opposing sunny and shady slopes, temperatures within the lower resolution pixel blocks of the thermal band are adjusted. The method improves the thermal variation due to topography within the block and is recommended for use in simple land-cover types where temperature variations due to topography are important. However, the method is inapplicable to nighttime images, and in flat terrain where any DN variation within a thermal block is solely due to the thermal properties of the surface. Most urban areas tend to occupy flatter ground and thermal variations due to topography may be of similar magnitude to those due to mixed land-cover. Differential reflectance intensity on opposing 3D building facets may be indistinguishable from low and high albedo urban surfaces, vegetation and shadows, and vertical surfaces are actually unseen on nadir images.

A simple method which is the subject of this paper may be termed Emissivity Modulation (EM). It was first used for microclimate analysis in Singapore (Nichol, 1994) with Landsat-5's 120 m resolution thermal band, and subsequently by Weng (2001) using Landsat ETM+ and Lu and Weng (2006) using ASTER. Thermal pixels of the high-resolution thermal sensors Landsat TM and ASTER correspond to pixel blocks comprising many visible band pixels (16 for Landsat TM and 36 for ASTER). The differential emissivity of land-cover types within a single larger pixel may be represented by applying known emissivity values to land-cover types classified from the higher resolution visible bands. The larger pixels of the blackbody temperature (**Tb**) image are combined with the emissivity values within each pixel block using Equation 1, and the resulting emissivity modulated image (**Ts**) has a pixel size corresponding to that of the higher resolution emissivity data:

$$\mathbf{Ts} = \mathbf{Tb}/\varepsilon^{1/4}. \quad (1)$$

The procedure is derived from the Stefan Boltzmann law ($M_b = \sigma T_s^4$), originally applicable to the radiant flux of black bodies (M_b), but which can be modified to pertain to the total spectral radiant flux of real materials (M_r) which are gray bodies (Equation 2):

$$M_r = \varepsilon \sigma T_s^4 \quad (2)$$

Where σ = Stefan Boltzmann constant (5.6697×10^{-8}Wm^{-2}K^{-4}), and ε = emissivity.

Then, if $M_b = \sigma\ T_s^4$, and $M_r = M_b$, then:

$$\sigma T_b^4 = \varepsilon \sigma T_s^4, \quad (3)$$

and Brightness Temperature (T_b) of an object can be related to its true Kinetic Temperature (T_s) by (Sabins, 1997):

$$T_b = \varepsilon^{1/4} (T_s), \quad (4)$$

Then, **Ts** may be derived from Equation 1.

The method described is not synonymous with image fusion techniques developed for visible wavelength images wherein both low- and high-resolution datasets comprise spectral radiance data of similar or overlapping wavelengths (Zhang, 2002; Nichol and Wong, 2005) which enable spatial detail to be maximized with minimal spectral (color) distortion. In the present case of thermal data, the high-resolution **Tb** values within each larger pixel block are merely adjusted for emissivity of different land-cover types, and it is assumed that temperatures within a large pixel vary only by cover type. Thus, the emissivity correction modulates the thermal values within the larger pixel block, but some distortion may be expected, since the temperature value of a small output pixel will still be influenced by the **Tb** values of surrounding cover types in the original lower resolution pixel block. This distortion would be greater for fragmented cover types. For example, an isolated patch of vegetation with a true Kinetic Temperature (**Ts**) of 15°C within an urban area of **Ts** = 21°C (Figure 1) belongs to a pixel block with brightness temperature (**Tb**) of 15°C. Following emissivity modulation, the **Ts** value of the vegetation patch would be slightly higher (17°C), but also higher than that of vegetation pixels whose original pixel block was dominated by vegetation and have a **Ts** of 16°C. Without emissivity modulation the vegetation pixel would have **Ts** of 21°C. Thus, the potential range of temperatures within any cover type may be artificially increased by the EM method. However, the method is physically sound and maintains the principle of energy conservation since the spatial average of the EM output pixels are equal to the **Ts** value of the whole block following emissivity correction at 90 m resolution. This point will be demonstrated later in the paper. Accuracy is also dependent on the extent to which the emissivities allocated represent the true emissivity values. The effectiveness of the EM method has not previously been verified due to the difficulty of obtaining adequate *in situ* surface temperatures.

Image and Field Data

The image used for the study was a nighttime scene of Hong Kong obtained at 22:41 local time on a clear night on 31 January 2007 (Figure 2). Band 13 (10.25 μm to 10.95 μm) of ASTER's five thermal bands was selected for processing since bands 10 and 14, being close to the edge of the atmospheric window, are most affected by atmospheric effects (Gillespie *et al.*, 1998), and the sensitivity of band 12 is said to be decreasing (ERSDAC, 2007). The image was obtained as Level 1B Radiance-at-Sensor data, uncorrected for emissivity or atmospheric effects. The noise-equivalent temperature difference (NEΔT) of the ASTER thermal bands is given as 0.3°C.

Eighteen paired surface and air temperature (**Ta**) measurements were taken in both urban and rural areas across

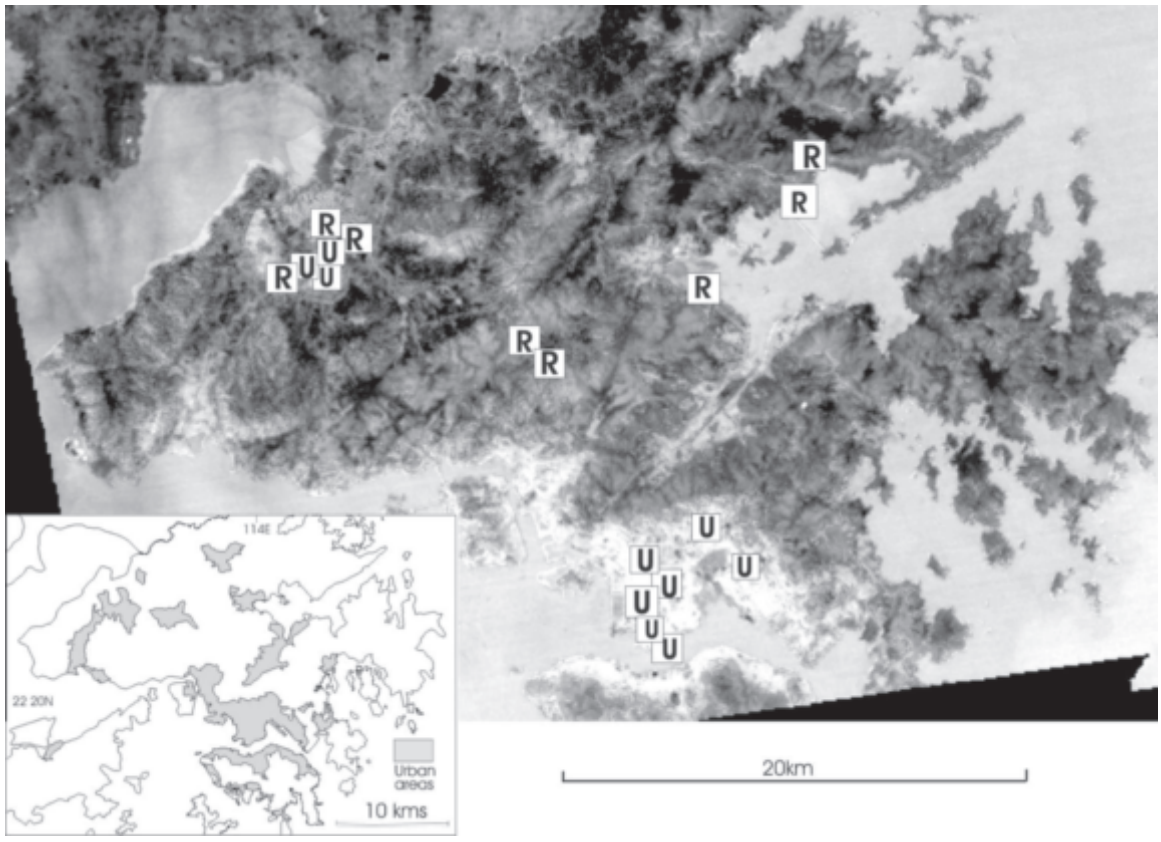

Figure 2. Location of ground data collection points over the thermal image of Hong Kong, on night of 31 January 2007: R = Rural, U = Urban. Urban areas of Hong Kong are shown as inset.

Kowloon and the New Territories, within one and one-half hours of the image time, 22:41 local time, with **Ta** offset by 1 m from the ground surface. Testo 720 portable digital thermometers with air and contact surface probes, having a stated accuracy of 0.2°C were used, and each measurement represented the average of three readings. Before fieldwork, all sensors were placed in the same room with an Omega CL7304A calibrator to measure the same temperature for 24 hours, and a certified mercury thermometer NIST SRM943 was used as a standard reference. Temperature outputs of all thermometers were then normalized according to the correlation between each sensor and the reference thermometer. All field measured air temperatures were normalized to the image time by reference to hourly air temperature data from the Hong Kong Observatory located near the center of the urban area.

Low wind speeds of approximately 1 m/sec. and low relative humidity of 55 percent were prevalent during image acquisition, and a temperature inversion was observed below 600 m altitude during the vehicle traverse. At the image time, dew point was below the field measured surface temperatures measured during fieldwork, so the probability of dew affecting surface emissivities was low. By the image time, mean surface temperatures had fallen to only 1.4°C above mean air temperature, suggesting that the inversion extended almost to the surface.

Methods

The image level 1B scaled radiance values were converted to actual radiance using the gain and offset values from the image metadata, and then to Brightness Temperature (**Tb**) using the Planck function (Figure 3).

The image was atmospherically corrected using *in situ* Sea Surface Temperature (SST) data, as the low atmospheric column water vapor amount of 2.3 cm at the image time and low aerosol optical thickness (AOT) (including water vapor) from an AERONET station located in the study area (AOT <0.3 at 0.65 μm) suggested that atmospheric absorption would be low. This, and the limited range of surface temperatures between 287°K and 294°K, suggest that the magnitude of the atmospheric correction would be small (see Price, 1983; Table 1), and only a little

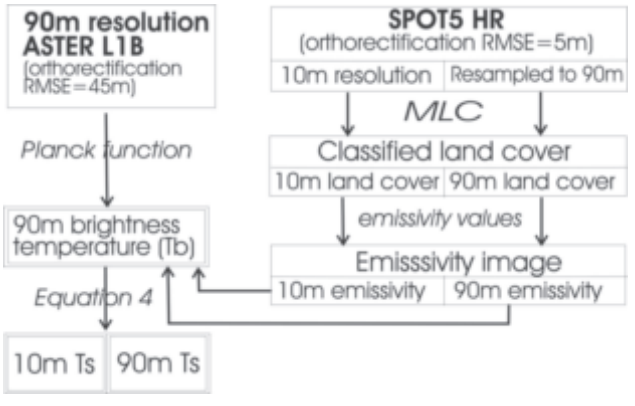

Figure 3. Methodology of the Emissivity Modulation procedure describing the derivation of an emissivity image from classification of a SPOT-5 HR image with 10 m resolution, and the combination of this with a 90 m ASTER image of brightness temperature.

TABLE 1. EMISSIVITY VALUES USED IN THE STUDY

Cover Type	Emissivity values used for Level 1B data*
Forest	0.97
Water	0.99
Dry Grassland	0.91
Other vegetation	0.97
Urban**	0.92
Soil/Sand	0.95

*Source: MODIS emissivity library, *http://www.icess.ucsb.edu/modis/EMIS/html/em.html*
**From field data measurement using methodology described in the text

in excess of 1°K. Furthermore, within the given range of temperatures the surface kinetic temperature is a linear function of brightness temperature (Price, 1983), thus differences in brightness temperature would not affect atmospheric absorption. In this case, the use of radiosonde data in a radiative transfer model may introduce more error than the magnitude of the correction (see also Chrysakoulas, 2003; Dousset and Gourmelon, 2003) An average of four SST measurements from the Hong Kong Observatory representing easterly and westerly waters of Hong Kong were used. These indicated that SST was temporally and spatially stable, at 290°K over the 12 hours before and after the image acquisition time. Based on these reference points having a mean image temperature of 291.6°K, atmospheric correction was performed by subtraction of the mean difference at these points (1.6°K) from the image. Since data from a local lidar station indicated that water vapor and aerosols were concentrated below the inversion height of approximately 600 m, a DEM was used and areas above the inversion were not corrected.

Since no visible wavebands were available for this nighttime scene, emissivity modulation according to land-cover type utilized a SPOT-5 image with 10 m resolution acquired on 31 December 2006, within one month of the ASTER image, and which was orthorectified to an RMSE of 0.5 pixel. The main land-cover types were classified using a Maximum Likelihood classifier from which an accuracy of 92 percent was achieved by comparing an additional set of training areas with a digital orthophoto having 0.5 m spatial resolution. Spectral emissivity values from the MODIS emissivity library (Table 1) were allocated to the classes. Since urban surfaces in Hong Kong, as in many tropical cities include more reflective surfaces such as glazed brick or light concrete having somewhat lower emissivities, a mean urban emissivity value was derived from field measurement of a range of urban surface types in the study area. A Raytec thermal radiometer operating in the range 8 μm to 14 μm was used for the measurement of black body temperature, and Testo 720 contact thermistors for surface measurement. The emissivity of 0.92 was derived from inversion of Equation 4. Surface temperature for the image (**Ts**) was then obtained by ratioing the emissivity image of 10 m resolution with the 90 m resolution **Tb** image in Equation 4, resulting in an output pixel size of 10 m.

The 10 m resolution emissivity modulated **Ts** image was then validated against the 18 field **Ts** measurements, along with the 90 m **Tb** and **Ts** images (Table 2). The field points were located by GPS, and the accuracy of corresponding coordinate on the images was determined by pixel

TABLE 2. COMPARISON OF *IN SITU* MEASURED SURFACE AND AIR TEMPERATURES WITH IMAGE DATA. MAD = MEAN ABSOLUTE DIFFERENCE

Field data	Image processing method	R^2	MAD
Surface field	**Tb** 90m	0.45	2.2
Surface field	**Ts** 90m	0.58	1.4
Surface field	**Ts** 10m (EM method)	0.71	1.0
Air field	Surface Field	0.66	1.4*
Air field	**Tb** 90m	0.31	
Air field	**Ts** 90m	0.56	
Air field	**Ts** 10m (EM method)	0.72	

*Mean Difference (MD)

size and the orthorectification accuracy of 0.5-pixel RMSE in all cases. The 90 m **Ts** image was derived from resampling and classifying the SPOT image at 90 m for which an accuracy of 80 percent was obtained for the land-cover classes.

Results

Air temperature measurements from the vehicle traverse and at the 18 sampling points (Table 3) indicate a well developed UHI of approximately 8°C between the most urbanized and most rural sites at the image time, and surface and air temperatures measured in the field were highly correlated ($R^2 = 0.66$) (Table 2). The processed image **Ts** values are close to the 18 *in situ* **Ts** measurements, suggesting the validity of the ASTER image radiance calibrations for Band 13, as well as the emissivity and atmospheric corrections used. Both **Ts** images (with pixel sizes of 10 m and 90 m, respectively) appear more accurate when compared with field measured **Ts** than the **Tb** image, but the EM image values are closest to the field data, with the lowest Mean Absolute Difference (MAD) of only 1.0°C, and for points falling within the urban area, an MAD of only 0.5°C. The EM image values were also the highest correlated with field **Ts** ($R^2 = 0.71$) compared with $R^2 = 58$ for the 90 m **Ts** image (Table 2).

The mean **Ts** values covering urban and rural areas, respectively, for the 90 m and 10 m **Ts** images are identical (Table 4), thus demonstrating that the EM maintains the principle of energy conservation since the spatial average of the EM output pixels are equal to the **Ts** value of the whole 90 m block following emissivity correction.

The greatest temperature contrast between different urban cover types was observed for the EM corrected image, with a mean difference of 3.5°C (Table 5), and this was accompanied by the lowest intra-class variability, with the EM image obtaining the lowest within-class standard deviations for all land-cover types (Table 5c). The closer correspondence of the EM image to land-cover is well illustrated in Plate 1, showing micro-scale temperature patterns within a 0.5 km^2 area. The extract is located on the north-east edge of the heat island core, where the old, high density commercial shopping district gives way to leafy low rise residential areas interspersed with parks and sports pitches (Plate 1b). Not only is the land-cover boundary more distinct on the EM image, but individual tree clusters and large buildings shown on the air photo (Plate 1b) can be identified by their temperatures at 10 m resolution (Plate 1a), whereas on the 90 m **Ts** image (Plate 1c) they are below the image resolution.

However, at meso-scale the overall magnitude, shape and distribution of the surface heat island (Plates 2a and 2b) is well defined on both the 10 m and 90 m **Ts** images. Both indicate a surface heat island magnitude of 7° to 8°C in the Kowloon Peninsula, and the north/south configuration of the heat island core (red and white areas representing **Ts** above 19.5°C on this winter night). These correspond to medium rise and very high-density commercial districts along the main shopping street, Nathan Road, with a few smaller outliers of similar structure and function to the north and east. Interspersion of the UHI by cooler parks, and lower density residential districts, and open spaces to the north/east and south/west of the Kowloon Peninsula can also be observed on both images.

For urban heat island analysis based on air temperature, the high correlation ($R^2 = 0.66$) in the field between surface and air temperatures at the image time suggests that image **Ts** would be highly correlated with **Ta**. This fact is supported, with $R^2 = 0.72$ for the EM image, which is substantially higher than the next highest, the 90 m **Ts** image with $R^2 = 0.56$ (Table 2).

TABLE 3. FIELD AND IMAGE TEMPERATURES (°C) AT THE 18 FIELD DATA COLLECTION POINTS SHOWN IN FIGURE 2: (R) = RURAL SITE, (U) = URBAN SITE

	Field data		Image data		
Location	Air	Surface	90m Tb	90m Ts	10m EM
concrete Tai Mo Shan (R)	14.0	14.2	12.0	14.1	15.0
grass Tai Mo Shan (R)	13.1	13.4	12.0	14.1	12.8
concrete Pier Plover Cove (R)	12.3	16.6	16.3	16.8	16.7
sand Plover Cove (R)	11.0	12.5	16.5	15.7	15.0
pond water Yuen Long (R)	13.0	16.4	11.8	13.2	13.5
river water Yuen Long (R)	12.1	17.0	14.6	14.9	16.2
grass Yuen Long park (R)	12.9	11.8	14.0	16.3	16.3
concrete car park.YL (U)	15.8	16.7	13.7	16.8	17.1
concrete Fook On bldg (U)	15.2	15.5	15.7	17.2	17.3
concreteYL Trade Ctr (U)	16.0	17.9	16.5	17.7	17.7
concrete Tolo Hwy (R)	14.1	15.3	16.1	15.3	15.5
concrete KMB depot (U)	17.5	19.6	17.7	18.9	18.9
concrete Kai Tak G bldg (U)	17.0	20.6	17.4	18.3	19.3
concrete Po Lin B. Mkok (U)	20.2	20.3	18.2	20.4	20.4
concrete Pres. bldg Mkok (U)	18.8	21.1	19.3	21.3	21.1
concrete Gold Plaza Mkok (U)	18.8	20.3	18.0	20.3	20.3
water Star Ferry (U)	19.5	17.4	15.2	19.6	17.2
concrete Star Ferry (U)	19.5	20.0	15.7	19.6	20.4

TABLE 4. STATISTICAL DIFFERENCES BETWEEN THE THREE PROCESSED IMAGES FOR URBAN AND RURAL AREAS

Urban			
Temperature statistic	90m **Tb**	90m **Ts**	10m **Ts**
mean	16.8	18.2	18.2
SD	2.3	2.3	2.3
max	21.6	22.9	21.3
min	8.1	9.4	7.8
Rural			
Temperature statistic	90m **Tb**	90m **Ts**	10m **Ts**
mean	13.8	15.2	15.2
SD	1.4	1.4	1.4
max	18.6	20.0	18.4
min	7.7	9.1	7.3

Discussion

The greater similarity of *in situ* surface temperatures to the EM image than to the 90 m **Ts** image may be largely due to the greater error in the initial image land-cover classification due to mixed pixels on the resampled 90 m SPOT image. This would lead to incorrect emissivity values, and thereby large temperature anomalies at 90 m scale. However, these are not so serious as to recommend no emissivity correction, as the 90 m **Tb** image was the least able to represent surface temperature. Thus overall, the study recommends the EM method for enhancing the spatial resolution of thermal sensors, and supports the observations of Li *et al.* (2004) that improved accuracy may be obtained from higher resolution thermal data. The decreased intra-class variance for all six land-cover types observed for the EM image is surprising in view of the spectral distortion resulting from the thermal characteristics of the original low-resolution pixel blocks, giving a potentially greater range of temperatures within any one cover type (Figure 1). It appears to be due to the higher resolution and the consequently fewer mixed pixels, since both 90 m images (with and without emissivity correction) have higher intra-class variability (SDs on Table 5).

On the other hand, greater temperature contrast between different land-cover types on the EM image appears to be due to the emissivity correction, not to increased spatial detail, since the uncorrected (**Tb**) image has much lower contrast than both the 10 m and 90 m **Ts** images. This is an expected result of emissivity correction using discrete land-cover data and has led to observations that the method creates sharp boundaries in the image (Wan, 1994; Gillespie *et al.*, 1999) and is thus inappropriate for study areas with gradual transitions such as rock and soil. However, urban areas are generally characterized by sharp land-cover boundaries. This is evident from the substantial (3.1° to 3.5°C) mean difference between cover types, even for the 90 m **Tb** image (with no emissivity correction) (Table 5).

The R^2 value of 0.72 between the EM image-based **Ts** and air temperature measured at the 18 ground points is higher than those obtained for the 90 m **Ts** and **Tb** images, which have R^2 of 0.56 and 0.31, respectively. This value is surprisingly high, given the fact that **Ta** is known to vary over larger distances than **Ts**. Indeed, Stoll and Brazel (1992) and Schmid *et al.* (1991) observe scales of approximately 250 m for urban air temperatures. The high correlation is perhaps explained by the observation that the surface heat island of 7° to 8°C at the image time is equal in magnitude to the UHI

TABLE 5. STATISTICAL DIFFERENCES BETWEEN THE THREE PROCESSED IMAGES FOR THE DIFFERENT URBAN COVER TYPES

a.	**90m Tb**						
Temperature statistic	forest	water	dry grassland	shrub land	urban	soil	Difference between means
mean	14.8	16.0	16.3	14.7	17.8	15.7	3.1
SD	1.4	1.7	2.0	2.2	1.8	2.1	
min	10.2	8.6	8.5	8.1	8.5	8.5	
max	20.4	20.8	21.1	20.8	21.6	20.9	
b.	**90m emissivity corrected**						
Temperature statistic	forest	water	dry grassland	shrub land	urban	soil	Difference between means
mean	16.2	17.3	17.7	16.0	19.2	17.1	3.2
SD	1.4	1.7	2.0	2.2	1.8	2.1	
min	11.5	10.0	9.8	9.4	9.9	9.8	
max	21.8	22.2	22.5	22.2	22.9	22.3	
c.	**10m emissivity modulated**						
Temperature statistic	forest	water	dry grassland	shrub land	urban	soil	Difference between means
mean	14.4	15.5	16.3	14.3	17.6	15.2	3.5
SD	1.3	1.7	1.9	2.1	1.8	1.9	
min	9.9	7.8	9.8	7.8	9.6	8.7	
max	18.6	19.3	21.1	19.1	21.3	20.0	

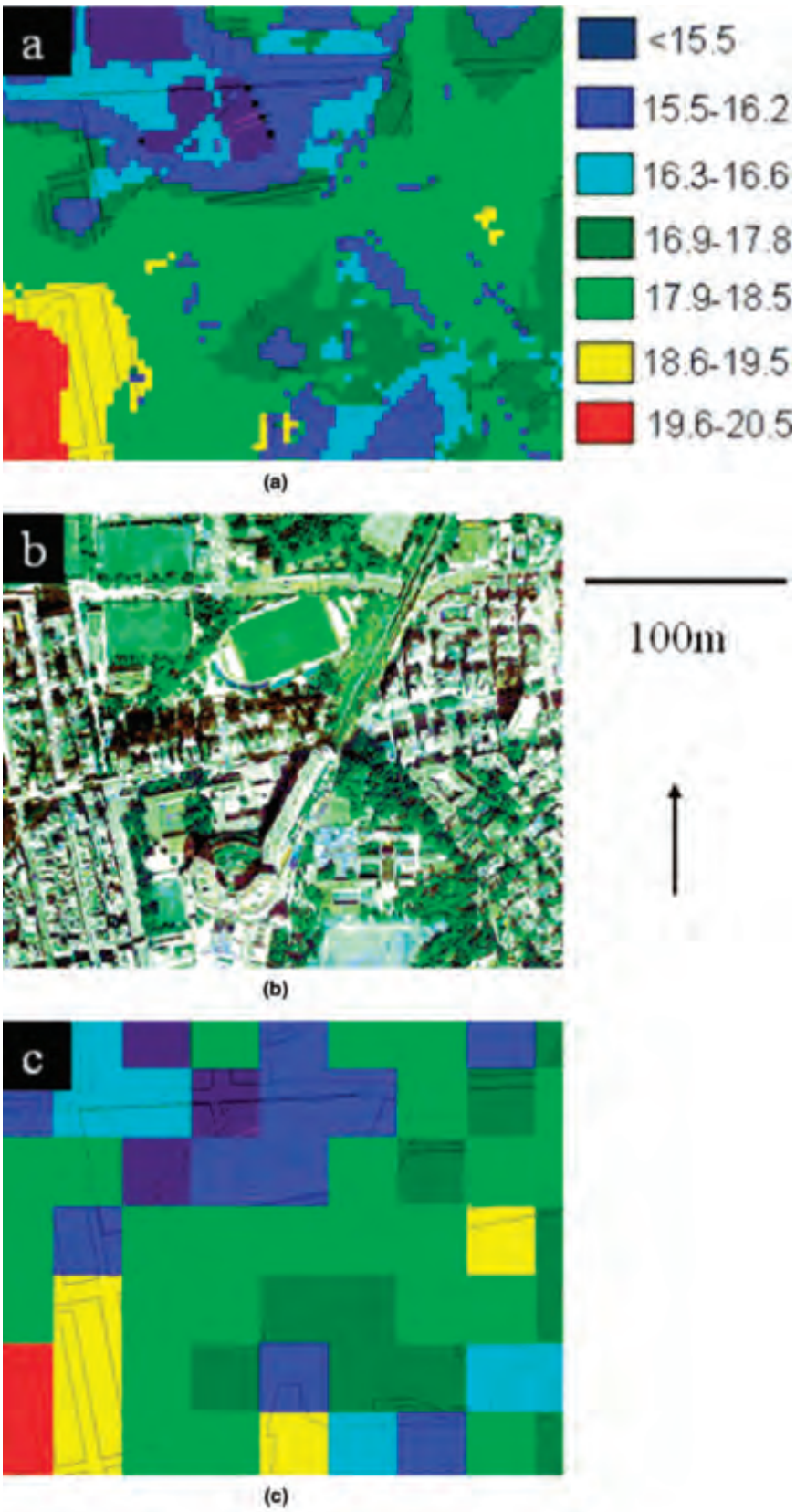

Plate 1. Image extract showing a 0.5 km ^{2} area at the north-east edge of the heat island core of Kowloon: temperatures in degrees Celsius: (a) Emissivity modulated (**Ts**) image, (b) color aerial photograph, and (c) 90 m emissivity corrected (**Ts**) image

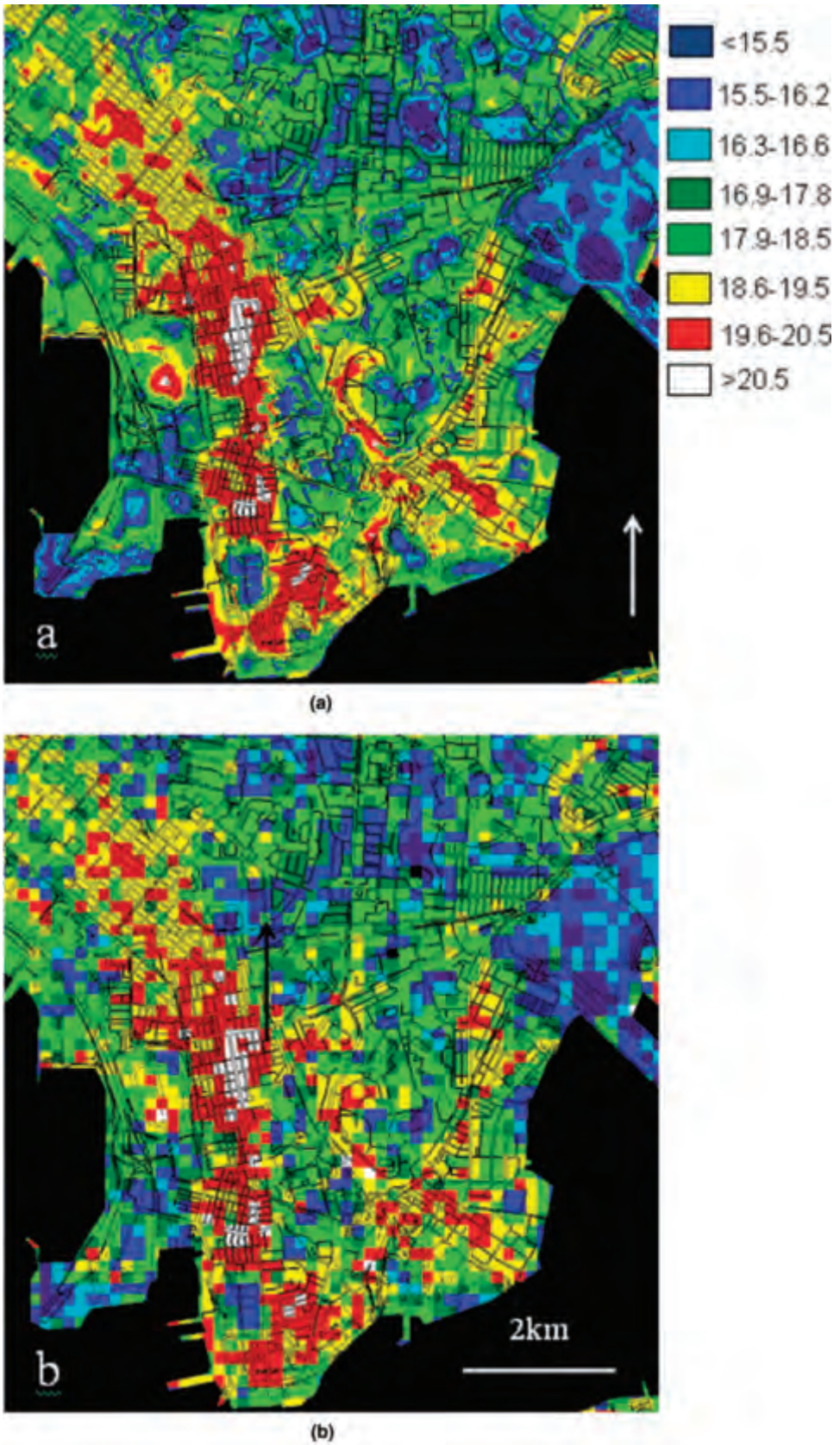

Plate 2. (a) Emissivity modulated image with 10 m pixels, and (b) Emissivity corrected image with 90 m pixels, showing the distribution of the surface heat island over Kowloon. Sea areas (black) are masked.

based on air temperatures, and further, that a mean difference of only 1.4°C between field measured surface and air temperatures was recorded (Table 2). This similarity of air and surface temperatures presumably results in low energy exchanges at the surface, decreased turbulence, and a consequently strong influence of the underlying surface on canopy layer air temperatures. However, the substantially higher correlation of the 10 m EM image with air temperature than the 90 m **Tb** image is also surprising given the recognized larger scale variability of air temperature, which was also noted on the mobile traverse conducted at the time. This may be explained by the mixed pixel problem in the image classification discussed above, leading to erroneous **Ts** values at 90 m resolution, and further supports the EM method.

Conclusions

The EM method is not only able to increase accuracy in the representation of surface temperatures, but is also better able to indicate the strong influence of land-cover type on the UHI, by showing greater temperature variation between classes and less variation within classes. This accords with Oke's (1976) Physical Structure model, which asserts that that the urban canopy layer heat island (i.e., at street level within urban canyons) is governed more by the immediate site character, especially building geometry and materials, than by thermally-modified air from upwind areas. In the Hong Kong context, this observation is directly applicable to current planning strategies as the older, medium rise, mixed commercial areas all coincide with heat island maxima, and should undergo redevelopment at lower density, using less absorptive materials, in order to mitigate increasingly oppressive temperatures. These areas are clearly identified as compact and homogeneous clusters on the EM image, but the boundaries are less precise on the 90 m **Ts** image.

The accuracy of the EM method depends on the accuracy of the land-use/land-cover data used as well as the emissivities derived from spectral libraries, which may not represent all surface types in the image. Furthermore, in urban areas individual surface emissivities may be less representative than "bulk" emissivities (Voogt and Oke, 2003), which would apply to scales larger than an individual component surface and take into account anisotropy of the image view angle, with occlusions and shadows due to the surface geometry. Although in theory, bulk emissivity can be computed if multiple thermal bands are available, the methods are often inaccurate due to non-linearity of the radiance-temperature relationship across wavebands, as well as low temperature contrasts at night. For most practical applications, if emissivity values retrieved from spectral libraries or from local field measurements can be applied to a higher resolution land-cover dataset, the EM method can achieve some improvements in the computation of kinetic temperature as well as the derivation of air temperatures, and microscale temperature patterns at individual building scale can be observed.

It is likely that the EM approach would be more successful at nighttime than in daytime, because differences in radiative temperature during daytime are more likely to be controlled by albedo (relative absorption of shortwave radiation), shading, moisture status or thermal properties, whereas at night, emissivity may become a stronger relative control.

Acknowledgments

The author would like to thank K.S. Lam, Fung Wing Yee, and Wong Man Sing for assistance with the field data and image processing, and CERG Grant No. B-Q01Q.

References

Chrysakoulas, N., 2003. Estimation of the all-wave urban surface radiation balance by use of ASTER multispectral imagery and in situ spatial data, *Journal of Geophysical Research*, 108:D18 4582, doi 10.1029/2003JD003896.

Collins, E.F., D.A. Roberts, and C.C. Borel, 2001. Spectral mixture analysis of simulated thermal infrared spectrometry data: An initial temperature estimate bounded TESSMA search approach, *IEEE Transactions on Geoscience and Remote Sensing*, 39:1435–1446.

Dousset, B., and F. Gourmelon, 2003. Satellite multi-sensor data analysis of urban surface temperatures and landcover, *ISPRS Journal of Photogrammetry and Remote Sensing* 58:43–54.

Dozier, J., 1981. A method for satellite identification of surface temperature fields of sub-pixel resolution, *Remote Sensing of Environment*, 11:221–229.

ERSDAC, 2007. URL: *www.gds.aster.ersdac.or.jp/gds_www2002/service_e/release_e/set_release_e.html*, (last date accessed: 19 January 2009).

Gillespie, A.R., S. Rokugawa, T. Matsunaga, S. Hook, and A.B. Kahle, 1998. A temperature and emissivity separation algorithm for advanced spaceborne thermal emission and reflection radiometer (ASTER) images, *IEEE Transactions on Geoscience and Remote Sensing*, 36:1113–1126.

Gillespie, A.R., S. Rokugawa, S. Hook, T. Matsunaga, and A.B. Kahle, 1999. *Temperature/Emissivity Separation Algorithm Theoretical Basis Document, Version 2.4*, NASA/GSFC, Greenbelt, Maryland.

Gillespie, A., 1992. Spectral mixture analysis of multispectral thermal infrared images, *Remote Sensing of Environment*, 42:137–145.

Goetz, S.J., 1997. A multisensor analysis of NDVI, surface temperature and biophysical variables at a mixed grassland site, *International Journal of Remote Sensing*, 18:71–94.

Guo, L.J., and J. McMoore, 1998. Pixel block intensity modulation: Adding spatial detail to TM band 6 thermal imagery, *International Journal of Remote Sensing*, 19:2477–2491.

Gustavson, W.T., R. Handcock, A.R. Gillespie, and H. Tonooka, 2003. An image sharpening method to recover stream temperatures from ASTER images, *Remote Sensing for Environmental Monitoring, GIS applications and Geology* (M. Ehlers, editor), *Proceedings of SPIE*, 4886:72–83.

Li, F., T.J. Jackson, W.P. Kustas, T.J. Schmugge, A.N. French, M.H. Cosh, and R. Bindlish, 2004. Deriving land surface temperature from Landsat 5 and 7 during SMEX02/SMACEX, *Remote Sensing of Environment*, 92:521–534.

Lu, D., and Q. Weng, 2006. Spectral mixture analysis of ASTER images for examining the relationship between urban thermal features and biophysical descriptors in Indianapolis, Indiana, USA, *Remote Sensing of Environment*, 104:157–167.

Nichol, J.E., 1994. A GIS based approach to microclimate monitoring in Singapore's high rise housing estates, *Photogrammetric Engineering & Remote Sensing*, 60(12):1225–1232.

Nichol, J.E, and M.S. Wong, 2005. Detection and interpretation of landslides using satellite images, *Land Degradation and Development*, 16:243–255.

Nichol. J.E., B.A. King, D. Quattrochi, I. Dowman, M. Ehlers, and X. Ding, 2007. Policy document on earth observation for urban planning and management, *Photogrammetric Engineering & Remote Sensing*, 73(9):973–979.

Oke, T.R., 1976. The distinction between canopy and boundary-layer heat islands, *Atmosphere*, 14:268–277.

Prata, A.J., 1994. Land surface temperature derived from the Advanced Very High Resolution Radiometer and the Along-Track Scanning radiometer-2: Experimental results and validation of AVHRR algorithms, *Journal of Geophysical Research*, 99(D6):13025–13058.

Price, J.C., 1983. Estimating surface temperatures from satellite thermal infra-red data - A simple formulation for the atmospheric effect, *Remote Sensing of Environment* 13:353–361.

Rigo, G., E. Parlow, and D. Oesch, 2006. Validation of satellite observed thermal emission with in-situ measurements over an urban surface, *Remote Sensing of Environment*, 104:201–210.

Sabins, F.F., 1997. *Remote Sensing Principles and Interpretation*, W.J. Freeman and Co., New York, 494 p.

Schmid, H.P., H.A. Cleugh, C.S.B. Grimmond, and T.R. Oke, 1991. Spatial variability of energy fluxes in suburban terrain, *Boundary Layer Meteorology*, 54:249–276.

Schmugge, T., S.J. Hook, and A.B. Kahle, 1995. TIMS observations of surface emissivity in Hapex-Sahel, *Proceedings of Geoscience and Remote Sensing Symposium, (IGARSS'95)*, 10–14 July, Firenze, Italy, Vol. 3, pp. 2224–2226.

Stoll, M.J., and A.J. Brazel, 1992. Surface-air temperature relationships in the urban environment of Phoenix, Arizona, *Physical Geography*, 13:160–179.

Ulivieri, C., C. Castronuovo, M. Francioni, R. Cardillo, 1992. *A Split Window Algorithm for Estimating Land Surface Temperatures Derived from Satellites*, Communication on Space Programs and Research, (COSPAR), Washington, D.C.

Valor, E., and V. Caselles, 1996. Mapping land surface emissivity from NDVI: Application to European, African and South American areas, *Remote Sensing of Environment*, 57:167–184.

Voogt, J.A., and T.R. Oke, 2003. Thermal remote sensing of urban climates, *Remote Sensing of Environment*, 86:370–384.

Weng, Q., 2001. A remote sensing-GIS evaluation of urban expansion and its impact on surface temperature in the Zhujiang Delta, China, *International Journal of Remote Sensing*, 22:1999–2014.

Weng, Q., D. Lu, and J. Schubring, 2004. Estimation of land surface temperature-vegetation abundance relationship for urban heat island studies, *International Journal of Remote Sensing*, 84:467–483.

Wan, Z., 1994. *MODIS Land Surface Temperature Algorithm Theoretical Basis Document (LST ATDB), Version 1*, Contract No. NAS5–31370, 37 p.

Zhang, Y., 2002. Problems in the fusion of commercial high-resolution satellite as well as Landsat 7 images and initial solutions, *International Archives of Photogrammetry and Remote Sensing* 34(4).